

## High-Latitude Galactic Emission in the *COBE* DMR Two-Year Sky Maps

A. Kogut<sup>1,2</sup>, A.J. Banday<sup>1</sup>, C.L. Bennett<sup>3</sup>, K.M. Górski<sup>4,5</sup>,  
G. Hinshaw<sup>1</sup>, and W.T. Reach<sup>4</sup>

*COBE* Preprint 95-09

Accepted for publication in *The Astrophysical Journal*

### ABSTRACT

We cross-correlate the *COBE*<sup>6</sup> DMR 2-year sky maps with spatial templates from long-wavelength radio surveys and the far-infrared *COBE* DIRBE maps. We place an upper limit on the spectral index of synchrotron radiation  $\beta_{\text{synch}} < -2.9$  between 408 MHz and 31.5 GHz. We obtain a statistically significant cross-correlation with the DIRBE maps whose dependence on the DMR frequencies indicates a superposition of dust and free-free emission. The high-latitude dust emission ( $|b| > 30^\circ$ ) is well fitted by a single dust component with temperature  $T = 18_{-7}^{+3}$  K and emissivity  $\epsilon \propto (\nu/\nu_0)^\beta$  with  $\beta = 1.9_{-0.5}^{+3.0}$ . The free-free emission is spatially correlated with the dust on angular scales larger than the  $7^\circ$  DMR beam, with *rms* variations  $5.3 \pm 1.8 \mu\text{K}$  at 53 GHz and angular power spectrum  $P \propto \ell^{-3}$ . If this correlation persists to smaller angular scales, free-free emission should not be a significant contaminant to measurements of the cosmic microwave anisotropy at degree angular scales for frequencies above 20 GHz.

*Subject headings:* radio continuum: interstellar – ISM: dust – cosmic microwave background

---

<sup>1</sup> Hughes STX Corporation, Laboratory for Astronomy and Solar Physics, Code 685, NASA/GSFC, Greenbelt MD 20771.

<sup>2</sup> E-mail: kogut@stars.gsfc.nasa.gov.

<sup>3</sup> Laboratory for Astronomy and Solar Physics, NASA Goddard Space Flight Center, Code 685, Greenbelt MD 20771.

<sup>4</sup> Universities Space Research Association, Laboratory for Astronomy and Solar Physics, Code 685, NASA/GSFC, Greenbelt MD 20771.

<sup>5</sup> On leave from Warsaw University Observatory, Aleje Ujazdowskie 4, 00-478 Warszawa, Poland

<sup>6</sup> The National Aeronautics and Space Administration/Goddard Space Flight Center (NASA/GSFC) is responsible for the design, development, and operation of the Cosmic Background Explorer (*COBE*). Scientific guidance is provided by the *COBE* Science Working Group. GSFC is also responsible for the analysis software and for the production of the mission data sets.

# 1. Introduction

The microwave sky is dominated by the cosmic microwave background (CMB) and Galactic synchrotron, dust, and free-free emission. A number of authors have attempted to distinguish these components based on sky surveys where one component dominates the others and on the frequency spectrum inferred from microphysical processes (Fixsen, Cheng, & Wilkinson 1983; Lubin et al. 1985; Wright et al. 1991; Bennett et al. 1992; Bensadoun et al. 1993; Gutiérrez de la Cruz et al. 1995). This approach has been most successful for synchrotron radiation: radio surveys and local measurements of the cosmic ray electron energy spectrum determine both the spectrum and morphology within broad limits (Banday & Wolfendale 1991, Bennett et al. 1992). Free-free emission from electron-ion interactions has well-determined spectral behavior but is poorly mapped at high Galactic latitudes (Bennett et al. 1992, Reynolds 1992). Dust emission suffers the opposite problem: although it dominates infrared surveys, its spectral behavior depends on the shape, composition, and size distribution of the dust grains, which are poorly known (Désert, Boulanger, & Puget 1990).

At millimeter wavelengths, the large angular scale anisotropy in the CMB is larger than fluctuations in the combined Galactic foregrounds, so that detailed Galactic modelling is not required for cosmological tests (Bennett et al. 1992, Smoot et al. 1992). At finer angular resolution or across a broader frequency band, this is not necessarily true (Banday & Wolfendale 1990, 1991; Franceschini et al. 1989). Precise maps of Galactic free-free and dust emission provide information on physical processes in the interstellar medium and aid planning of future CMB anisotropy measurements.

Synchrotron emission results from the acceleration of cosmic-ray electrons in the Galactic magnetic field, and may be approximated as a power law in frequency,  $T_{\text{synch}} \propto \nu^\beta$ . Bennett et al. (1992) review several models of synchrotron emission based on radio surveys at 408 MHz (Haslam et al. 1981) and 1420 MHz (Reich & Reich 1988). They consider three models for the spectral index: spatially invariant, spatially varying but frequency-independent, and a spatially varying index that steepens with frequency as determined by the local cosmic-ray energy spectrum. Comparison with a survey at 19 GHz (Boughn et al. 1992) suggests that the third model is somewhat better than the other two, although all have obvious shortcomings. Synchrotron indices used by various authors to scale the 408 MHz survey to millimeter wavelengths range from -2.7 to -3.1, corresponding to a factor of 7 uncertainty in amplitude at 53 GHz.

Bennett et al. (1992, 1994a) provide a full-sky map of the Galactic free-free emission derived from linear combinations of the *COBE* Differential Microwave Radiometers (DMR) sky maps, designed to isolate emission with  $T_{\text{ff}} \propto \nu^{-2.15}$ . Although in principle this map presents an unbiased full-sky template for emission from the ionized gas in the interstellar medium, in practice the noise levels are such that only the quadrupolar component  $\Delta T \propto \csc |b|$  is detected at  $|b| > 15^\circ$ . Other tracers of the warm ionized medium suffer from signal to noise ratio (e.g., NII emission,

Bennett et al. 1994b) or from undersampling and selection biases (e.g., H $\alpha$  emission and pulsar dispersion measure, Reynolds 1992, 1984).

Wright et al. (1991) provide estimates of far-infrared Galactic dust emission using the *COBE* Far Infrared Spectrophotometer (FIRAS). Assuming that the dust intensity along each line of sight may be characterized by optically thin emission with frequency-dependent emissivity  $I_\nu = \tau_0 (\frac{\nu}{\nu_0})^\beta B_\nu(T)$  where  $B_\nu$  is the Planck function and  $\nu_0 = 900$  GHz, they find temperature  $T = 23.3$  K and emissivity  $\beta = 1.65$  for the mean spectrum including the Galactic plane. A fit with  $\beta$  fixed at 2 shows excess emission at long wavelengths, characterized by a two-temperature model with  $T_1 \approx 20.4$  K and  $T_2 \approx 4.8$  K. Reach et al. (1995a) extend this model with an improved data set; at high latitudes ( $|b| > 30^\circ$ ) they detect a pervasive long wavelength excess characterized by either a flattened emissivity  $\beta = 1.2 \pm 0.3$  or a combination of warm and cold components with  $T_1 = 17.6 \pm 0.5$  K and  $T_2 = 6.9 \pm 0.8$  K. The opacities of the warm and cold components are highly correlated; however, the FIRAS data do not distinguish between two distinct (although spatially correlated) dust populations or a single dust population with enhanced submillimeter emissivity.

Attempts to measure Galactic emission at millimeter wavelengths are hindered by the small amplitude of the individual emission components and the presence both of other Galactic sources and of anisotropy in the cosmic microwave background. Point-by-point decomposition based on the different frequency dependences of the emission mechanisms are typically limited by signal to noise considerations (Brandt et al. 1994). The ability to detect weak signals is significantly enhanced if the angular distribution is known *a priori*. In this paper, we cross-correlate the DMR full-sky maps with spatial templates from long-wavelength radio surveys and the far-infrared maps of the *COBE* Diffuse Infrared Background Experiment (DIRBE, Boggess et al. 1992). After accounting for instrument noise and chance alignments of the CMB anisotropy, we derive upper limits to the synchrotron spectral index steeper than used by many authors. We obtain a statistically significant cross-correlation with the DIRBE maps whose dependence on the DMR frequencies indicates a superposition of dust and free-free emission. The dust temperature and emissivity derived from angular variations in the DMR and DIRBE data agree with the values derived independently from the absolute FIRAS spectra, and place a lower limit on enhanced dust emissivity at long wavelengths. The detection of free-free emission correlated with the DIRBE dust emission provides a spatial template and normalization for at least one component of the warm ionized medium at various angular scales.

## 2. Analysis

We assume that the DMR microwave maps may be represented by a superposition of CMB anisotropy and Galactic signals whose angular distribution is traced by an external map,

$$\Delta T^{\text{DMR}} = \Delta T^{\text{CMB}} + \alpha \Delta X^{\text{Gal}},$$

where  $\Delta T^{\text{DMR}}$  is the antenna temperature<sup>7</sup> in a DMR map (in units mK),  $\Delta X^{\text{Gal}}$  is the intensity of the Galactic template map (not necessarily in temperature units), and the coefficient  $\alpha$  converts the units of the Galactic map to antenna temperature at the DMR frequency. Fitting for  $\alpha$  on a pixel-by-pixel basis (e.g., a linear correlation coefficient) does not make full use of the angular information in the two maps; instead, we compare the full cross-correlation function

$$C(\theta) = \sum_{i,j} \Delta X_i^{\text{Gal}} \Delta T_j^{\text{DMR}}$$

(summed over all pixel pairs  $\{i, j\}$  separated by angle  $\theta$ ) to the autocorrelation function

$$A(\theta) = \sum_{i,j} \Delta X_i^{\text{Gal}} \Delta X_j^{\text{Gal}}$$

and find the coefficient  $\alpha$  by minimizing

$$\chi^2 = \sum_{a,b} (C - \alpha A)_a (\mathbf{M}^{-1})_{ab} (C - \alpha A)_b$$

where  $\mathbf{M}$  is the covariance matrix of the cross-correlation function, and the indices  $a$  and  $b$  run over the angular bins of the correlation functions. Bennett et al. (1993) use the same technique to search for correlation between the DMR maps and various extragalactic sources.

We use the 2-year DMR sky maps (Bennett et al. 1994a) at 9.5, 5.7, and 3.3 mm wavelength (31.5, 53, and 90 GHz). For long wavelength (synchrotron) Galactic templates, we use either the 408 MHz survey (Haslam et al. 1981) or the 408 MHz survey scaled to the DMR frequencies using a spatially varying frequency-dependent spectral index as described in Bennett et al. (1992), denoted here as the ‘‘cosmic ray’’ model. For short wavelength (dust) Galactic templates, we use the DIRBE sky maps at 240, 140, and 100  $\mu\text{m}$  wavelength from which a model of the zodiacal dust emission has been removed (Reach et al. 1995b). We convolve the Galactic template maps with the DMR beam pattern (Wright et al. 1994) and pixelize them in the same Galactic representation used for the DMR maps.

The Galactic plane has considerable structure smaller than the  $7^\circ$  DMR beam size; we exclude the Galactic plane ( $|b| < 20^\circ$  or  $|b| < 30^\circ$ ) from all analysis. The DMR maps are insensitive to a monopole and have a dipole dominated by the CMB.

---

<sup>7</sup> Antenna temperature  $T_A$  is defined in terms of the power received per unit bandwidth,  $P = kT_A \Delta\nu$  where  $k$  is Boltzmann’s constant. It is related to the intensity  $I_\nu$  by  $I_\nu = 2kT_A \frac{\nu^2}{c^2}$ .

Galactic microwave emission from synchrotron, free-free, and dust is dominated by a  $\csc|b|$  quadrupole. Analysis which includes the quadrupole could result in a false positive cross-correlation between the DMR maps and a Galactic template due to the microwave emission from a different template with a brighter quadrupole at millimeter wavelengths. Furthermore, the CMB quadrupole has a component counter-aligned with a Galactic cosecant of similar magnitude (Bennett et al. 1992), potentially masking correlation between the DMR and Galactic maps. Accordingly, we remove the monopole, dipole, and quadrupole from the the high-latitude portion of both the DMR and Galactic template maps prior to computing the auto- and cross-correlation functions. As a consequence, our results depend only on the intensity variations in the maps and are insensitive to the zero level of either the DMR or Galactic template maps.

We determine the covariance matrix  $\mathbf{M}$  of the cross-correlation function and assess the statistical significance of the coefficient  $\alpha$  as Galactic features occasionally align with CMB anisotropy by using Monte Carlo simulations in which the DMR map is replaced by a scale-invariant Harrison-Zel'dovich spectrum of CMB anisotropy normalized to the quadrupole value  $Q_{rms-PS} = 20 \mu\text{K}$  determined from the 2-year DMR data (Górski et al. 1994). To each CMB realization we add a realization of instrument noise defined by the level and pattern of noise in the DMR A and B channels, then combine the channels to form the (A+B)/2 sum map. We excise the Galactic plane and remove the monopole, dipole, and quadrupole from each simulated sum map prior to computing the cross-correlation. The mean coupling between angular bins defines the covariance matrix,  $\mathbf{M}_{ab} = \frac{1}{N} \sum C_a C_b$  averaged over  $N$  simulations; throughout this work we use 72 angular bins each of width  $2^\circ 6'$ . The simulations thus automatically account for cosmic variance from random alignments of CMB anisotropy with features in the Galactic template maps as well as the effect of instrument noise and the aliasing of power between multipole moments in the quadrupole-removed maps. Cosmic variance dominates the uncertainty in the fitted  $\alpha$ ; consequently, we weight each pixel uniformly when computing the cross-correlation function.

We test for possible biases in the cross-correlation technique by analyzing 2000 additional simulations which include a signal  $T^{\text{sim}} = 0.002 \text{ mK MJy}^{-1} \text{ sr } I^{\text{DIRBE}}$  in addition to the CMB and noise. We recover a mean coefficient  $\langle \alpha \rangle = (1.96 \pm 0.03) \times 10^{-3} \text{ mK MJy}^{-1} \text{ sr}$  at  $|b| > 20^\circ$ , in excellent agreement with the simulation input. We have also repeated the analysis using the cross power spectra and obtained coefficients  $\alpha$  in agreement with those found using the cross correlation function  $C(\theta)$ .

### 3. Results

Table 1 shows the fitted coefficient  $\alpha$  from the cross correlation of the DMR 2-year maps with various Galactic template maps, compared to 2000 random realizations of CMB and instrument noise. We detect no statistically significant correlation between the DMR maps and any synchrotron template: the amplitude of any signal with the the 408 MHz survey or the cosmic-ray synchrotron model is smaller than the noise in the DMR maps. All of the DMR maps show a statistically significant correlation with the DIRBE far-infrared maps, indicating a detection of signal with common spatial structure in the high-latitude portion of the two data sets.

The correlation coefficients are averages over the high-latitude sky and do not provide specific information on individual patches of the sky. We estimate the amplitude of the signal at each DMR frequency by multiplying the standard deviation of the Galactic template maps (after quadrupole subtraction) by the fitted coefficients  $\alpha$ . Since the three DIRBE maps trace the same warm dust emission, the DIRBE templates provide nearly identical estimates of Galactic emission at each of the DMR frequencies. The uncertainties in the fitted coefficients  $\alpha$  between any one DMR map and the three DIRBE maps are dominated by the noise and CMB signal in the DMR maps, and are not statistically independent. We therefore adopt the unweighted average of the fitted signal at each DMR frequency, with uncertainty estimated by the smallest uncertainty of the three DIRBE cross-correlations.

Table 2 shows the estimated Galactic signal in the DMR maps traced by the two synchrotron templates and the DIRBE dust morphology. The Galactic signal correlated with the DIRBE dust distribution has *rms* fluctuations  $\Delta T_{\text{Gal}} = 7.1 \pm 3.4 \mu\text{K}$  antenna temperature at  $|b| > 30^\circ$  and  $7^\circ$  angular resolution in the most sensitive 53 GHz channels. For comparison, the *rms* instrument noise at 53 GHz is  $98 \mu\text{K}$ . Galactic emission is a minor contribution to the brightness fluctuations at millimeter wavelengths. Specifying the template of the Galactic emission allows a significant increase in sensitivity to faint extended emission.

Since the DIRBE maps are dominated by infrared dust emission, it is natural to interpret the correlated DMR–DIRBE signal as evidence for dust emission at millimeter wavelengths. However, the sharp rise in signal amplitude at 53 and 31.5 GHz is inconsistent with emission by dust alone. The amplitude (in antenna temperature) of emission traced by the DIRBE maps more than doubles between 53 and 31.5 GHz, requiring some emission component with negative spectral index. The spectral index  $T \propto \nu^\beta$  of the signal, without modelling any components, is  $\beta = -1.7 \pm 0.4$  between the 31.5 and 53 GHz data and  $\beta = -1.5 \pm 0.9$  between the 53 and 90 GHz data (68% confidence), suggestive of an admixture of dust ( $\beta \approx +2$ ) and free-free ( $\beta = -2.15$ ) emission, but inconsistent with dust emission only.

The DMR–DIRBE signals are not appreciably affected by synchrotron emission ( $\beta_{\text{synch}} \approx -3.1$  at millimeter wavelengths). Direct cross-correlation of the DMR maps with either the 408 MHz survey or the cosmic-ray synchrotron model shows no statistically significant signal. The fitted coefficients for the 408 MHz survey at

$|b| > 20^\circ$  are significant only at 90% confidence, and have a spectrum closer to the CMB than to synchrotron emission (Table 2). The 408 MHz coefficients all become negative at the higher cut  $|b| > 30^\circ$ , which we take as further evidence that the correlations at  $|b| > 20^\circ$  are dominated by chance alignment of the CMB with a feature in the 408 MHz survey. Similarly, there is no compelling evidence for synchrotron emission in the 2-year DMR maps with spatial template traced by the cosmic-ray model. We adopt an upper limit for either model  $\Delta T_{\text{synch}} < 12 \mu\text{K}$  (95% confidence) for fluctuations in synchrotron emission at 31.5 GHz.

Cross-correlations between the DIRBE maps and the 408 MHz survey provide further evidence that the rising signal in the low-frequency DMR channels is not caused by synchrotron emission. We cross-correlate the DIRBE and 408 MHz template maps (with the 408 MHz survey scaled to 53 GHz using a spectral index  $\beta = -3$  to provide direct comparison with the DMR 53 GHz results) and obtain a fitted coefficient at  $|b| > 30^\circ$ ,  $\alpha_{\text{synch}} = 3 \times 10^{-5} \text{ mK MJy}^{-1} \text{ sr}$ , two orders of magnitude smaller than the correlation observed between the DMR and DIRBE maps. Synchrotron emission at high latitude does not strongly correlate with the DIRBE far-infrared dust emission.

We conclude that synchrotron emission does not account for the observed correlation between the high-latitude DMR and DIRBE sky maps, leaving free-free emission as the most likely alternative. We decompose the sky signals from Table 2 into dust and free-free components assuming  $\beta = 2$  for the dust. Table 3 shows the *rms* dust and free-free normalization at 53 GHz. Approximately half of the high-latitude Galactic signal in the DMR 90 GHz data results from dust and half from free-free emission, while the 53 GHz data are dominated by free-free emission. Free-free emission increases markedly at the lower Galactic cut. Note that  $|b| > 20^\circ$  includes emission from the Orion and Ophiuchus complexes, which contain substantial amounts of ionized gas. The increase in fitted free-free amplitude when regions known to contain ionized gas are included in the analysis provides further support for the existence of free-free emission spatially correlated with the infrared dust emission.

Tables 1 and 2 demonstrate a significant detection of dust and free-free emission in the high-latitude DMR data. We may use the combined DIRBE and DMR data to limit dust emission properties at long wavelengths. We fit the *rms* DIRBE and DMR signals to dust models of the form  $I_\nu = \tau(\frac{\nu}{\nu_0})^\beta B_\nu(T) + A_{\text{ff}}(\frac{\nu}{\nu_0})^{-0.15}$  (model 1) or  $I_\nu = \tau_1(\frac{\nu}{\nu_0})^2 B_\nu(T_1) + \tau_2(\frac{\nu}{\nu_0})^2 B_\nu(T_2) + A_{\text{ff}}(\frac{\nu}{\nu_0})^{-0.15}$  (model 2), i.e., a model with a single dust population with enhanced submillimeter emissivity or a two-temperature model with  $\nu^2$  emissivity. Both models include a free-free emission term  $A_{\text{ff}}$ . Figure 1 shows the spectra of the intensity fluctuations and the fitted dust and free-free emission for a single dust component (model 1) at  $|b| > 20^\circ$ . Figure 2 shows the  $\chi^2$  contours of this model in the temperature-emissivity plane. The best fit occurs for dust temperature  $T = 18_{-7}^{+3} \text{ K}$  and  $\beta = 1.9_{-0.5}^{+3.0}$  with  $\tau = (1.2_{-0.5}^{+2.5}) \times 10^{-5}$  (68% confidence), in agreement with the absolute FIRAS spectra (Wright et al. 1991, Reach et al. 1995a). The DMR data place a lower limit to a frequency-dependent dust emissivity over the wavelength range 6 mm to 100  $\mu\text{m}$ :  $\beta > 1.2$  at 95% confidence.

The two-component dust model is not significantly constrained by the DMR-DIRBE cross-correlation. Provided one component is near 18 K, changes in the temperature of the cold component are compensated by correlated variations in opacity. We may fix the temperatures in model 2 to the values derived from the FIRAS  $|b|>30^\circ$  spectra and compare the opacities derived from fluctuations in the warm and cold components to the total opacities derived from FIRAS (Table 4). The opacities for both the warm and cold components derived from the DMR-DIRBE cross-correlation are smaller than the corresponding values derived from the FIRAS spectra, as expected if the dust emission contains a significant monopole or quadrupole term.

Figure 3 summarizes the contribution of various Galactic emission mechanisms (standard deviation of each component averaged over  $|b|>30^\circ$ ) at  $7^\circ$  angular resolution. The width of each band reflects the 68% confidence level uncertainty in the amplitude of each component, and includes the absolute calibration uncertainty of the template maps. The “cosmic-ray” synchrotron model provides a modestly better fit to the available low-frequency data than the 408 MHz survey scaled with a spatially invariant spectral index (Bennett et al. 1992). Accordingly, we normalize the synchrotron curve in Figure 3 by the cross-correlation of the DMR 31.5 GHz channel with the cosmic-ray model, as indicated by the filled circle. Fluctuations in the synchrotron emission at DMR frequencies are modestly smaller than expected; the cosmic-ray model predicts  $\Delta T_{\text{synch}} = 13 \mu\text{K}$  at  $|b|>30^\circ$  in the 31.5 GHz map. We note that our results are insensitive to the zero level of the radio surveys, which can influence the amplitude of the predicted fluctuations through a monopole change in the spectral index. The 95% confidence level upper limit on synchrotron emission ( $\Delta T_{\text{synch}} < 12 \mu\text{K}$  at 31.5 GHz) is the same for both the cosmic-ray and 408 MHz templates, and may be used to set an upper limit on the high-latitude synchrotron spectral index:  $\beta_{\text{synch}} < -2.9$  between 408 MHz and 31.5 GHz.

Free-free emission is normalized by the free-free values in Table 2 and dominates fluctuations in diffuse synchrotron emission for frequencies above 20 GHz. The dust spectrum inferred from the DMR-DIRBE cross-correlation is in agreement with more precise spectra from the *COBE* FIRAS experiment. The dust model in Figure 3 represents a range of high-latitude spectra from  $T_{\text{dust}} = 21$  K and  $\beta_{\text{dust}} = 1.4$  to  $T_{\text{dust}} = 16$  K and  $\beta_{\text{dust}} = 2$ , with opacity normalized to the spatial variation of the DIRBE 240  $\mu\text{m}$  map. The upper limits on dust emission at millimeter wavelengths from the DMR-DIRBE cross-correlation dust model (after removing the free-free component) are also shown.

## 4. Discussion

A significant result of this analysis is the detection of fluctuations in the microwave sky brightness with the angular variation of the DIRBE far-infrared maps and the frequency spectrum of free-free emission. The angular structure in the far-infrared maps is dominated by interstellar dust associated with atomic gas (Boulanger & Pérault 1987). Our results suggest that the ionized component of the interstellar medium is at least partially correlated with the atomic gas.

Previous comparisons of the  $H\alpha$  recombination line from the ionized gas revealed no clear correlation with the HI hyperfine line from the neutral gas (Reynolds 1987), although one filament detected in  $H\alpha$  may be related to a parallel offset structure in HI (Reynolds et al. 1995). Similar correlated structures, as well as evaporating surfaces of clouds embedded in a hot ionized gas (*cf* McKee & Ostriker 1977) could account for the correlation we observe between the dust and free-free emission. The *rms* variation in the inferred free-free emission at 53 GHz is  $\Delta T_{\text{ff}} = 5.3 \pm 1.8 \mu\text{K}$  at  $7^\circ$  angular resolution, averaged over the high-latitude sky ( $|b| > 30^\circ$ ) after removal of the quadrupole component. The amplitude of this signal compares favorably with the predicted signal  $\Delta T_{\text{ff}} \approx 7 \mu\text{K}$  inferred from fluctuations in  $H\alpha$  emission (Reynolds 1992), where for convenience we reference  $\Delta T_{\text{ff}}$  to 53 GHz.

The detection of free-free emission correlated with the DIRBE far-infrared maps provides a template for at least one component of Galactic free-free emission. We may place an upper limit for the combined free-free emission from all sources by forming a linear combination of the DMR maps designed to pass emission with spectral index -2.15, cancel emission with a CMB spectrum, and minimize instrument noise:

$$T_{\text{ff}} = 0.40 \times \frac{1}{2}(T'_{31A} \pm T'_{31B}) - 0.09 \times \frac{1}{2}(T'_{53A} \pm T'_{53B}) - 0.37 \times \frac{1}{2}(T'_{90A} \pm T'_{90B}),$$

where  $T'$  is the antenna temperature in each DMR channel after subtracting synchrotron and dust emission using the cosmic-ray and DIRBE models, respectively. Since both synchrotron and dust are small compared to the free-free emission at 53 GHz (Figure 3), their residual contribution after correction is negligible. This linear combination has only 33% larger noise than the most sensitive 53 GHz channels. We smooth the maps with a  $7^\circ$  FWHM Gaussian to reduce further the effects of noise, remove a fitted quadrupole, and compare the variance of the (A+B)/2 sum map to the (A-B)/2 difference map to obtain an estimate for the free-free fluctuations  $\Delta T_{\text{ff}} = 3.9 \pm 5.7 \mu\text{K}$ , in excellent agreement with the value  $\Delta T_{\text{ff}} = 5.1 \pm 1.6 \mu\text{K}$  from the DMR-DIRBE cross-correlation at the same  $10^\circ$  effective smoothing. Free-free emission from sources uncorrelated with the far-infrared dust emission, although present at high latitudes, does not dominate the component correlated with the dust emission for the range of angular scales probed here.

Figure 4a shows the power spectrum of the inferred free-free emission at 53 GHz. We calculate the power spectrum of the high-latitude DIRBE 240  $\mu\text{m}$  map using a set of basis functions orthonormal on the region  $|b| > 30^\circ$  (Górski 1994), and

normalize to free-free emission at 53 GHz using the correlation coefficient derived from a dust/free-free decomposition of the correlation coefficients from Table 1,  $\alpha_{\text{ff}} = (3.35 \pm 1.11) \times 10^{-3} \text{ mK MJy}^{-1} \text{ sr}$ . The power falls rapidly at small angular scales:

$$P_{\text{ff}} = \frac{8a_2}{\ell^3},$$

where  $P(\ell) = \frac{1}{2\ell+1} \sum_m a_{\ell m}^2$  is the mean power at multipole order  $\ell$  ( $\ell \approx \pi/\theta$ ), and the quadrupole normalization  $a_2 = (6.02 \pm 3.99) \mu\text{K}^2$ . The power spectrum in Figure 4 is an average over the high-latitude sky. On smaller angular scales, Gautier et al. (1992) estimate the dust power spectrum using  $8^\circ \times 8^\circ$  IRAS patches and find  $P \propto \ell^{-3}$  as well.

The DMR and DIRBE data provide the normalization for the correlated free-free emission on angular scales larger than  $7^\circ$ . The  $\ell^{-3}$  dust power spectrum continues to smaller angular scales, and it is plausible that the spatial correlation between the dust and the warm ionized gas also persists. We thus estimate the *rms* free-free fluctuations on various angular scales by integrating the free-free power spectrum in Figure 4a over the range in  $\ell$  corresponding to the patch size and the Gaussian beam width. Table 5 compares the model predictions to H $\alpha$  and radio measurements. An H $\alpha$  map of a single  $12^\circ \times 10^\circ$  patch suggests *rms* variations  $\Delta T_{\text{ff}} = 1.4 \mu\text{K}$  at  $0.8^\circ$  angular resolution (Reynolds 1992). Similar observations of a  $7^\circ \times 7^\circ$  patch at  $0.1^\circ$  angular resolution yield an upper limit of  $\Delta T_{\text{ff}} < 1.2 \mu\text{K}$  (Gaustad et al. 1995), while deep VLA observations at  $1'$  resolution provide an upper limit  $\Delta T_{\text{ff}} < 1.3 \mu\text{K}$  (Fomalont et al. 1993). There is generally good agreement between observations and the power spectrum predictions, suggesting that the dominant free-free emission is correlated with the dust and that the correlation persists to smaller angular scales.

If the free-free/dust correlation does persist to smaller angular scales, it has interesting implications for experiments measuring CMB anisotropy at degree angular scales. Measurements of CMB anisotropy must contend with the problem of estimating the foreground Galactic emission and removing it if it contributes a significant fraction of the CMB anisotropy. Since no template for the free-free emission exists, experimenters typically observe in several frequency bands and use a linear combination of the angular anisotropy at different frequencies to remove any emission with the free-free emission spectrum. Although this removes the foreground emission, it increases the noise in the corrected CMB results, often to the point of obscuring the CMB signal. If free-free emission could be demonstrated to be a negligible contaminant, significant reductions in noise could be realized.

Table 5 shows the free-free power spectrum predictions for two cases of interest. A full-sky map at 53 GHz with angular resolution  $0.5^\circ$  would observe *rms* free-free emission of  $6.1 \pm 2.0 \mu\text{K}$  averaged over the high-latitude sky after quadrupole subtraction. Surveys restricted to smaller regions exclude power from Fourier modes with wavelength larger than the survey size. A  $10^\circ \times 10^\circ$  survey (corresponding to modes  $\ell > 18$ ) with angular resolution  $0.5^\circ$  would measure *rms* free-free emission of  $1.5 \pm 0.5 \mu\text{K}$ , where the quoted errors reflect only the uncertainty in the free-

free normalization and do not include the variation from patch to patch on the sky. Emission at this level is well below the expected magnitude of CMB anisotropy, although individual patches may show free-free emission significantly larger than the high-latitude average.

The small amplitude of the free-free signal explains why no structure is observed in the maps of free-free emission derived from linear combinations of the two-year DMR maps. The instrument noise in the free-free map presented above is 20 times larger than the free-free signal estimated from the DMR–DIRBE cross-correlation. Figure 4b shows the power spectrum of this free-free map, including the uncertainty from instrument noise. It is clear that the noise per multipole order  $\ell$  is much larger than the signal. The increase in sensitivity required to detect signals at the few  $\mu\text{K}$  level results from the *a priori* specification of the DIRBE map as a spatial template for the emission.

The high-latitude Galactic signal is small compared to the CMB anisotropy in the DMR maps and does not significantly alter previously published estimates based on the uncorrected DMR 53 GHz sky maps. The standard deviation at  $7^\circ$  angular resolution of the combined CMB and Galactic signals at  $|b| > 30^\circ$  is  $\Delta T_{\text{sky}} = 42.6 \pm 8.4 \mu\text{K}$  antenna temperature at 53 GHz. The CMB and Galactic signals are uncorrelated; correcting  $\Delta T_{\text{sky}}$  for the estimated Galactic signal  $\Delta T_{\text{Gal}} = 7.1 \pm 3.4 \mu\text{K}$  yields an estimated CMB anisotropy  $\Delta T_{\text{CMB}} = 42.0 \pm 8.6 \mu\text{K}$ , within  $0.7 \mu\text{K}$  (7% of the statistical uncertainty) of the uncorrected result. The CMB anisotropy may also be characterized by a power-law distribution of primordial density perturbations  $P(k) \propto k^n$  with quadrupole normalization  $Q_{rms-PS}$  and index  $n$ . Removing the Galactic emission traced by the DIRBE maps changes  $Q_{rms-PS}$  or  $n$  by less than 0.3 standard deviations, well within their respective statistical uncertainties.

## 5. Conclusions

We detect statistically significant cross-correlation between the *COBE* two-year DMR maps and the DIRBE 240, 140, and 100  $\mu\text{m}$  maps. The *rms* amplitude of the correlated Galactic signal in the DMR maps at  $|b| > 30^\circ$ , after quadrupole subtraction, is  $15.6 \pm 6.0$ ,  $7.1 \pm 3.4$ , and  $3.9 \pm 3.8 \mu\text{K}$  at 31.5, 53, and 90 GHz, corresponding to dust emission  $\Delta T_{\text{dust}} = 0.9 \pm 1.3 \mu\text{K}$  and free-free emission  $\Delta T_{\text{ff}} = 5.3 \pm 1.8 \mu\text{K}$  at 53 GHz and  $7^\circ$  angular resolution. The dust emission may be used to put a lower limit on the emissivity at millimeter wavelengths,  $\Delta T_{\text{dust}} \propto \nu^\beta$  with  $\beta > 1.2$  at 95% confidence. The dust temperature and emissivity derived from fluctuations in the DMR and DIRBE maps are in agreement with values derived from the absolute FIRAS spectra at wavelengths between the DMR and DIRBE coverage. Similar analyses using the 408 MHz survey or a model of synchrotron emission based on the 408 MHz survey with spatially varying, frequency-dependent spectral index yielded upper limits for fluctuations in synchrotron emission of  $\Delta T_{\text{synch}} < 12 \mu\text{K}$  at 31.5 GHz, corresponding to a spectral index  $\beta_{\text{synch}} < -2.9$  between 408 MHz and 31.5 GHz.

We detect a component of Galactic free-free emission correlated with the DIRBE maps, providing a template for the angular distribution of free-free emission on angular scales larger than the  $7^\circ$  DMR beam. The *rms* variations in this correlated component,  $\Delta T_{\text{ff}} = 5.3 \pm 1.8 \mu\text{K}$ , are in good agreement with the *rms* variations from *all* sources of free-free emission,  $\Delta T_{\text{ff}} = 3.9 \pm 5.7 \mu\text{K}$ , derived from a linear combination of the DMR 2-year maps. Extrapolating the power spectrum of the free-free emission to smaller angular scales yields an estimated contribution for *rms* fluctuations at  $0.5^\circ$  angular scale observed at 53 GHz of  $\Delta T_{\text{ff}} = 6.1 \pm 2.0 \mu\text{K}$  for a full-sky map at  $|b| > 30^\circ$ , or  $\Delta T_{\text{ff}} = 1.5 \pm 0.5 \mu\text{K}$  for observations restricted to a  $10^\circ \times 10^\circ$  patch.

If the spatial correlation between the dust and warm ionized gas observed on large angular scales persists to smaller angular scales, free-free emission should not be a serious contaminant to measurements of the medium-scale CMB anisotropy. It is worth pointing out, however, that small regions of the sky have variations much larger than the standard deviation over the full sky. If free-free emission is correlated with dust emission on all angular scales of interest, the IRAS or DIRBE maps may be used to estimate both dust and free-free emission in individual regions of the sky.

## References

- Banday, A. & Wolfendale, A.W. 1991, MNRAS, 248, 705  
— 1990, MNRAS, 245, 182  
Bennett, C.L., et al. 1994a, ApJ, 436, 423  
— 1994b, ApJ, 434, 587  
— 1993, ApJ, 414, L77  
— 1992, ApJ, 396, L7  
Bensadoun, M., Bersanelli, M., De Amici, G., Kogut, A., Levin, S.M., Limon, M., Smoot, G.F., & Witebsky, C. 1993, ApJ, 409, 1  
Boggess, N.W., et al. 1992, ApJ, 397, 420  
Boughn, S.P., Cheng, E.S., Cottingham, D.A., & Fixsen, D.J., 1992, ApJ, 391, L49  
Boulanger, F. & Péroult, M. 1987, ApJ, 330, 964  
Brandt, W.N., Lawrence, C.R., Readhead, A.C.S., Pakianathan, J.N., & Fiola, T.M. 1994, ApJ, 424, 1  
Désert, F.-X., Boulanger, F., & Puget, J.-L. 1990, A&A, 327, 215  
Fomalont, E.B., Partridge, R.B., Windhorst, R.A., & Lowenthal, J.D. 1993, ApJ, 404, 8  
Fixsen, D.J., Cheng, E.S., & Wilkinson, D.T. 1983, PRL, 50, 620  
Franceschini, A., Toffolatti, L., Danese, L., & De Zotti, G. 1989, ApJ, 344, 35  
Gaustad, J.E., Oh, E.S., McCullough, P.R., & Van Buren, D. 1995, BAAS, 27, 823  
Gautier, T.N., Boulanger, F., Péroult, M., & Puget, J.L. 1992, AJ, 103, 1313  
Górski, K.M. 1994, ApJ, 430, L85  
Górski, K.M., Hinshaw, G., Banday, A.J., Bennett, C.L., Wright, E.L., Kogut, A., Smoot, G.F., & Lubin, P. 1994, ApJ, 430, L89  
Gutiérrez de la Cruz, C.M., Davies, R.D., Rebolo, R., Watson, R.A., Hancock, S., & Lasenby, A.N. 1995, ApJ, 442, 10  
Haslam, C.G.T., Klein, U., Salter, C.J., Stoffel, H., Wilson, W.E., Cleary, M.N., Cooke, D.J., & Thomasson, P. 1981, A&A, 100, 209  
Lubin, P., Villela, T., Epstein, G., & Smoot, G. 1985, ApJ, 298, L1  
McKee, C.F. & Ostriker, J.P. 1977, ApJ, 218, 148  
Reach, W.T., et al. 1995a, ApJ, 451, 188  
Reach, W.T., Franz, B.A., Kelsall, T., & Weiland, J.L. 1995b, *Unveiling the Cosmic Infrared Background*, ed. E. Dwek, (New York:AIP)  
Reich, P., & Reich, W. 1988, A&AS, 74, 7  
Reynolds, R.J., Tufte, S.L., Kung, D.T., McCullough, P.R., & Heiles, C. 1995, ApJ, (submitted)  
Reynolds, R.J. 1992, ApJ, 392, L35  
— 1987, ApJ, 323, 118  
— 1984, ApJ, 282, 191  
Smoot, G.F., et al. 1992, ApJ, 396, L1  
Wright, E.L., et al. 1994, ApJ, 420, 1  
— 1991, ApJ, 381, 200

Table 1: DMR-Galactic Template Cross-Correlation Coefficients<sup>a</sup>

Template Map	DMR Map	$10^3 \alpha ( b  > 20^\circ)$	$10^3 \alpha ( b  > 30^\circ)$
408 MHz <sup>b</sup>	31.5 GHz	$2.32 \pm 1.57$	$-0.70 \pm 2.25$
	53 GHz	$1.54 \pm 0.91$	$-0.28 \pm 1.31$
	90 GHz	$1.14 \pm 1.00$	$-0.068 \pm 1.43$
Cosmic-Ray <sup>c</sup>	31.5 GHz	$(0.21 \pm 0.40) \times 10^3$	$(0.63 \pm 0.46) \times 10^3$
	53 GHz	$(0.13 \pm 0.93) \times 10^3$	$(0.78 \pm 1.07) \times 10^3$
	90 GHz	$(3.83 \pm 5.25) \times 10^3$	$(-2.24 \pm 5.95) \times 10^3$
DIRBE 240 $\mu\text{m}^d$	31.5 GHz	$12.63 \pm 1.80$	$10.09 \pm 3.65$
	53 GHz	$5.61 \pm 1.03$	$4.03 \pm 2.06$
	90 GHz	$2.34 \pm 1.20$	$2.34 \pm 2.28$
DIRBE 140 $\mu\text{m}^d$	31.5 GHz	$9.27 \pm 1.33$	$7.38 \pm 2.90$
	53 GHz	$4.06 \pm 0.77$	$3.90 \pm 1.70$
	90 GHz	$1.82 \pm 0.86$	$1.47 \pm 1.83$
DIRBE 100 $\mu\text{m}^d$	31.5 GHz	$18.06 \pm 2.54$	$14.57 \pm 6.03$
	53 GHz	$6.88 \pm 1.40$	$6.46 \pm 3.45$
	90 GHz	$2.76 \pm 1.61$	$4.56 \pm 3.89$

<sup>a</sup> The antenna temperature at each DMR frequency of Galactic emission traced by template map X is  $T_A = \alpha X$  mK (see text).

<sup>b</sup>  $\alpha$  has units mK K<sup>-1</sup> since the template map has units K.

<sup>c</sup>  $\alpha$  is dimensionless since the template map has units mK.

<sup>d</sup>  $\alpha$  has units mK (MJy/sr)<sup>-1</sup> since the template map has units MJy sr<sup>-1</sup>.

Table 2: RMS Galactic Signal in DMR Sky Maps

Template Map	DMR Frequency (GHz)	$rms$ at $ b >20^\circ$ ( $\mu\text{K}$ )	$rms$ at $ b >30^\circ$ ( $\mu\text{K}$ )
408 MHz	31.5	$7.6 \pm 5.1$	$-1.9 \pm 6.1$
	53	$5.0 \pm 3.0$	$-0.8 \pm 3.6$
	90	$3.7 \pm 3.3$	$-1.9 \pm 3.9$
Cosmic-Ray	31.5	$2.9 \pm 5.4$	$8.0 \pm 5.8$
	53	$0.3 \pm 2.8$	$2.2 \pm 3.0$
	90	$2.4 \pm 3.2$	$-1.3 \pm 3.5$
DIRBE	31.5	$35.2 \pm 4.9$	$15.6 \pm 6.0$
	53	$14.8 \pm 2.7$	$7.1 \pm 3.4$
	90	$6.3 \pm 3.1$	$3.9 \pm 3.8$

Table 3: Free-Free and Dust Antenna Temperature at 53 GHz

Component	$rms$ at $ b >20^\circ$ ( $\mu\text{K}$ )	$rms$ at $ b >30^\circ$ ( $\mu\text{K}$ )
Free-Free	$12.0 \pm 1.5$	$5.3 \pm 1.8$
Dust	$1.1 \pm 1.1$	$0.9 \pm 1.3$

Table 4: Dust Opacities in Two-Component Model,  $|b|>30^\circ$

Data Set	Warm Opacity $10^5 \tau_1$	Cold Opacity $10^5 \tau_2$
FIRAS <sup>a</sup>	$2.18 \pm 0.03$	$15.0 \pm 0.7$
DMR-DIRBE <sup>b</sup>	$0.87 \pm 0.08$	$2.3^{+11}_{-2.3}$

<sup>a</sup> FIRAS values derived from mean dust spectra (Reach et al. 1995a).

<sup>b</sup> DMR-DIRBE values derived from intensity fluctuations.

Table 5: Free-Free Observations and Model Predictions<sup>a</sup>

Angular Resolution	Patch Size	Observed $\Delta T_{\text{ff}}$	Predicted $\Delta T_{\text{ff}}^b$	Reference
10°	$ b  > 30^\circ$	$3.9 \pm 5.7$	$5.3 \pm 1.6$	This work
0°8	$12^\circ \times 10^\circ$	1.4	$1.5 \pm 0.5$	Reynolds 1992
0°1	$7^\circ \times 7^\circ$	$< 1.2$	$1.4 \pm 0.5$	Gaustad et al. 1995
1'	$7' \times 7'$	$< 1.3$	$0.15 \pm 0.05$	Fomalont et al. 1993
0°5	$10^\circ \times 10^\circ$	—	$1.5 \pm 0.5$	—
0°5	$ b  > 30^\circ$	—	$6.1 \pm 2.0$	—

<sup>a</sup> All free-free values are in  $\mu\text{K}$  antenna temperature at 53 GHz

<sup>b</sup> *rms* fluctuations estimated from power spectrum of free-free emission correlated with DIRBE dust emission (see text).

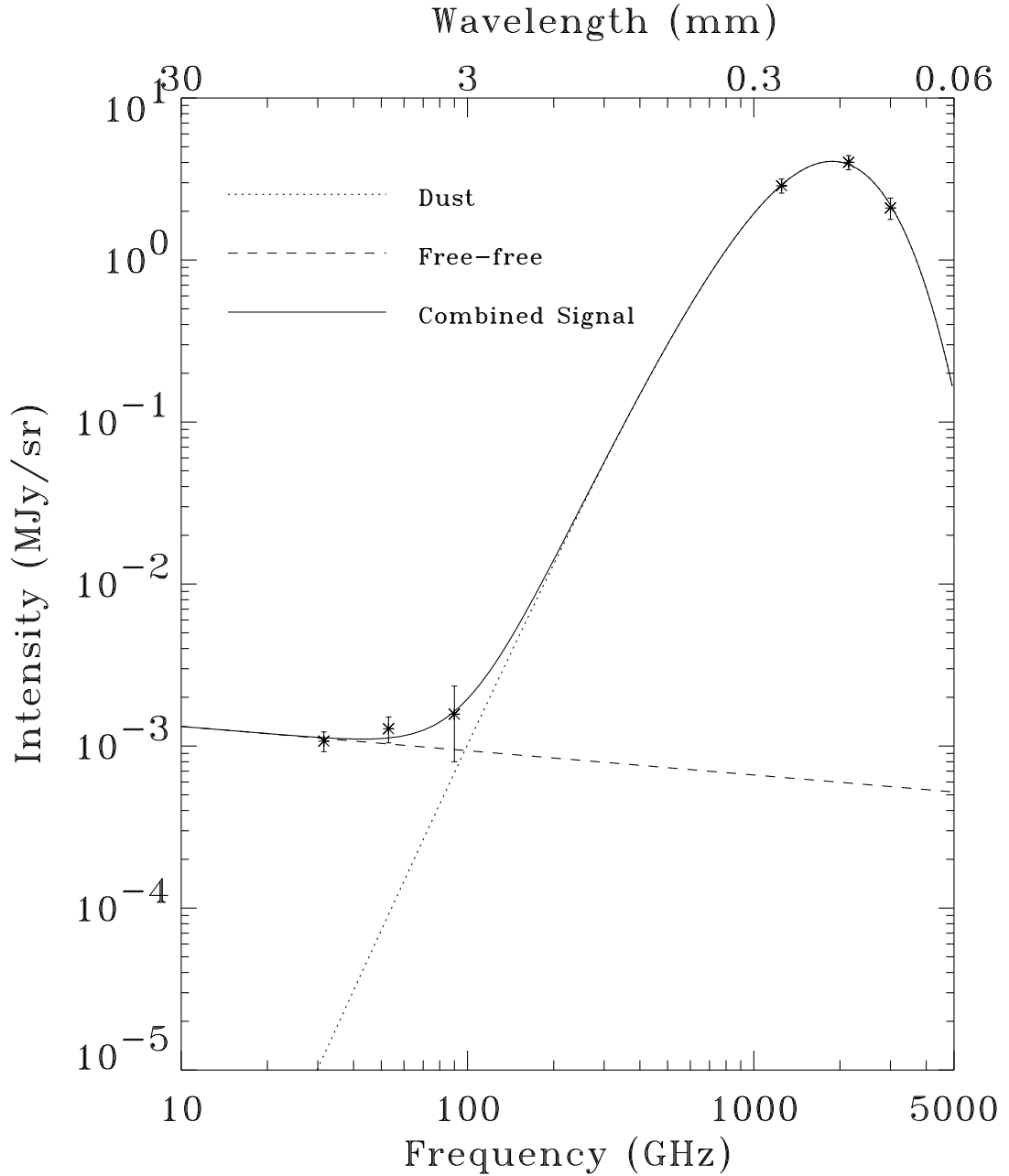


Figure 1: Spectrum of correlated intensity fluctuations in the DMR and DIRBE data at  $|b| > 20^\circ$ . Far-infrared points represent the standard deviation of the DIRBE maps after subtracting a fitted monopole, dipole, and quadrupole, and include calibration uncertainties. Long-wavelength points are the values inferred from the cross-correlation of the DMR and DIRBE maps (Table 2). The fitted free-free emission and single-component dust model are also shown.

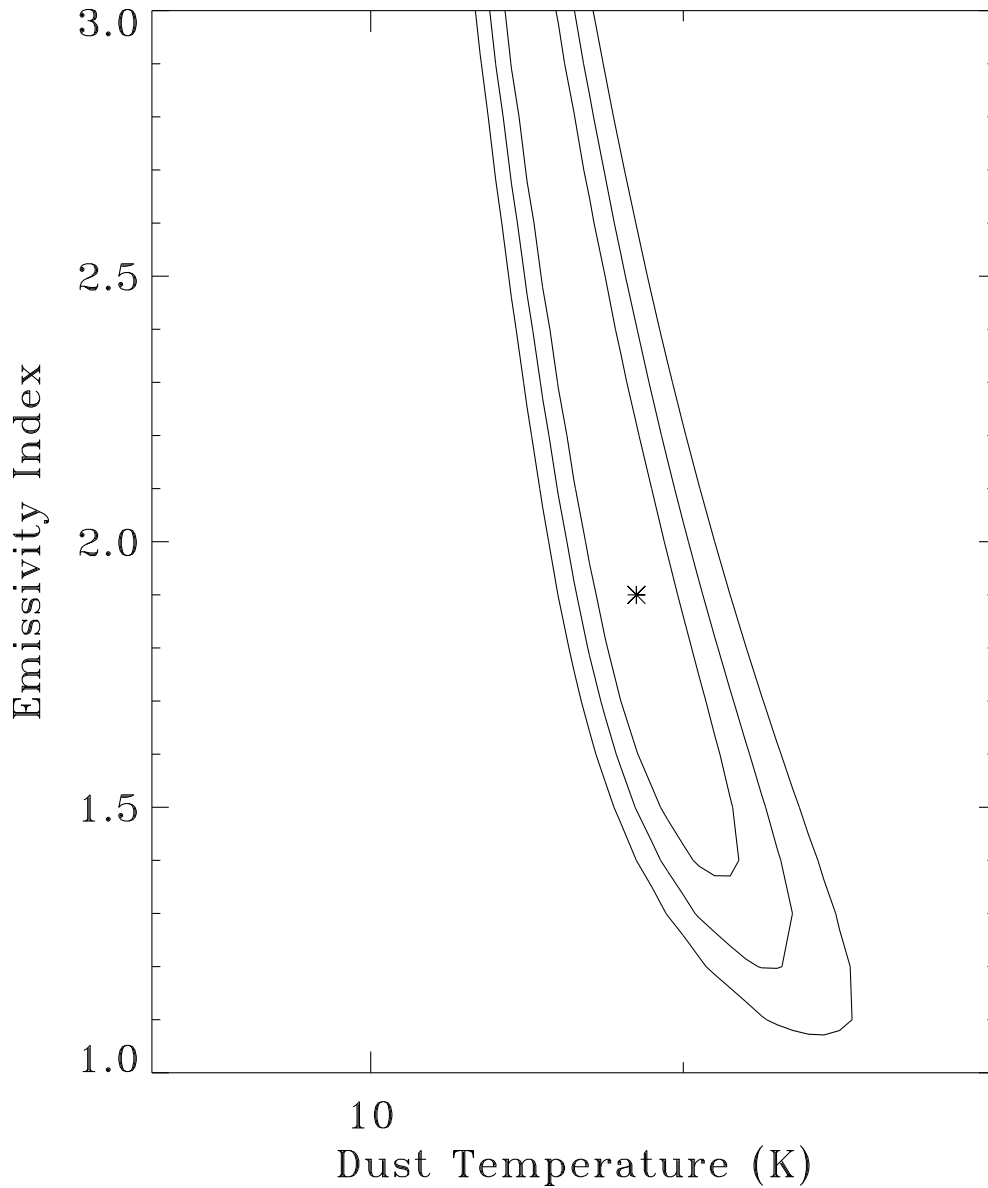


Figure 2:  $\chi^2$  contours for the temperature and emissivity index of a single dust component fitted to the DMR–DIRBE intensity fluctuations at  $|b|>20^\circ$ . The asterisk marks the best fitted value. Free-free emission is fitted separately for each value of the dust emissivity.

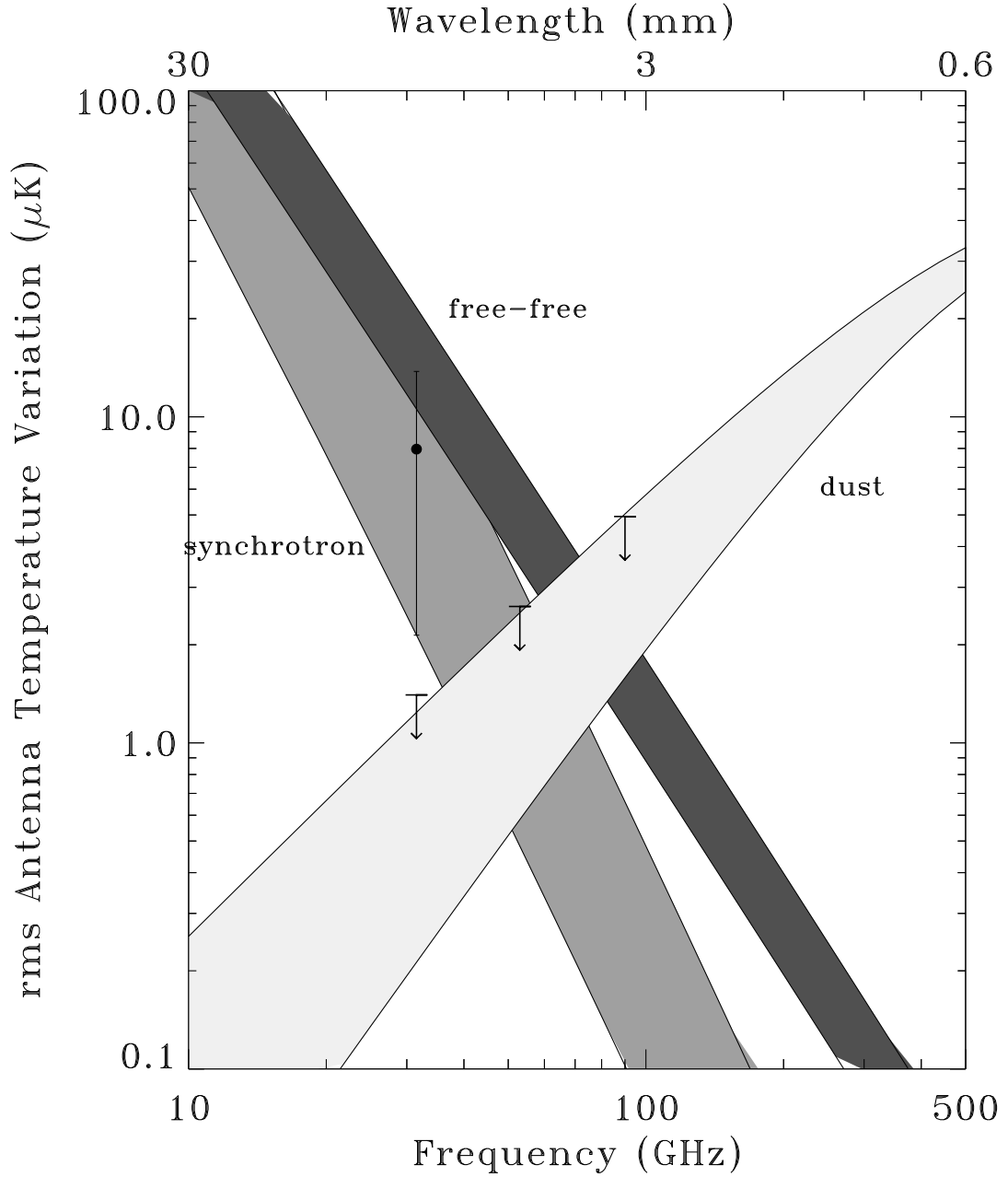


Figure 3: Frequency spectra of high-latitude Galactic emission (*rms* fluctuations at  $|b| > 30^\circ$  after quadrupole subtraction for a  $7^\circ$  FWHM beam). Free-free emission dominates synchrotron emission at frequencies above 20 GHz. Upper limits on dust emission at millimeter wavelengths from the DMR–DIRBE cross-correlation, after correction for free-free emission, are also shown.

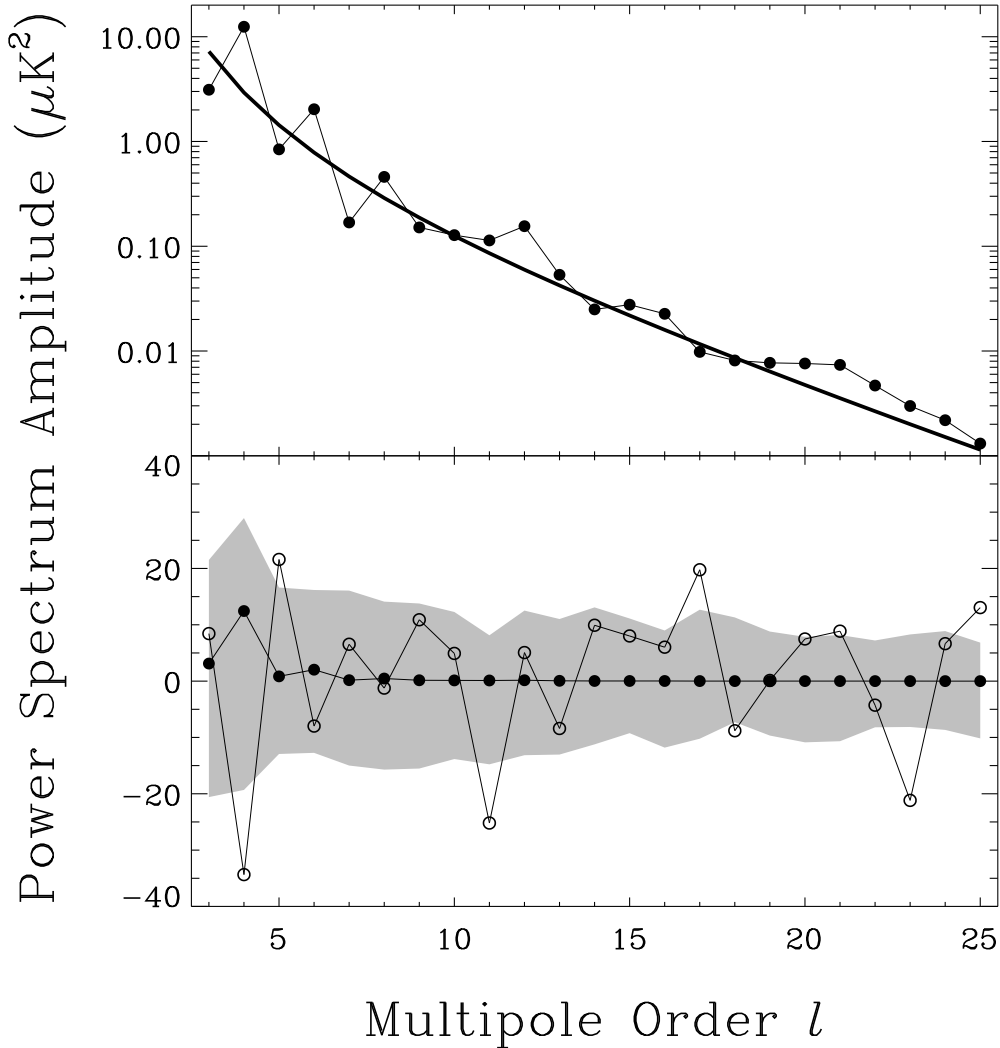


Figure 4: Mean power spectrum of the inferred free-free emission at 53 GHz. (top) Free-free power spectrum derived from the DMR–DIRBE cross-correlation at Galactic latitude  $|b| > 30^\circ$ . The filled circles show the DIRBE power spectrum on angular scales larger than  $7^\circ$ , normalized to the correlation coefficient of the free-free emission at 53 GHz (see text). The solid line shows a fitted  $\ell^{-3}$  spectrum. (bottom) Mean power spectrum of a free-free map derived from a linear combination of DMR maps *without* specifying the DIRBE maps as the spatial template. Open circles are the actual power at each multipole order, while the grey band shows the 68% confidence interval from instrument noise. Filled circles are the power spectrum of the DMR–DIRBE cross-correlation from the top panel. The free free signal is buried in the instrument